



HAL
open science

Autopsy of an eruptive phase of Tungurahua volcano (Ecuador) through coupling of seismo-acoustic and SO₂ recordings with ash characteristics

J. Battaglia, S. Hidalgo, B. Bernard, A. Steele, S. Arellano, K. Acuña

► To cite this version:

J. Battaglia, S. Hidalgo, B. Bernard, A. Steele, S. Arellano, et al.. Autopsy of an eruptive phase of Tungurahua volcano (Ecuador) through coupling of seismo-acoustic and SO₂ recordings with ash characteristics. *Earth and Planetary Science Letters*, 2019, 511, pp.223-232. hal-02015784

HAL Id: hal-02015784

<https://uca.hal.science/hal-02015784>

Submitted on 22 Oct 2021

HAL is a multi-disciplinary open access archive for the deposit and dissemination of scientific research documents, whether they are published or not. The documents may come from teaching and research institutions in France or abroad, or from public or private research centers.

L'archive ouverte pluridisciplinaire **HAL**, est destinée au dépôt et à la diffusion de documents scientifiques de niveau recherche, publiés ou non, émanant des établissements d'enseignement et de recherche français ou étrangers, des laboratoires publics ou privés.



Distributed under a Creative Commons Attribution - NonCommercial 4.0 International License

1 **Autopsy of an eruptive phase of Tungurahua volcano**
2 **(Ecuador) through coupling of seismo-acoustic and SO₂**
3 **recordings with ash characteristics**

4
5 **J. Battaglia**^{1,*}, **S. Hidalgo**², **B. Bernard**², **A. Steele**^{3,2}, **S. Arellano**⁴, **K. Acuña**²
6

7 ¹ Université Clermont Auvergne, CNRS, IRD, OPGC, Laboratoire Magmas et Volcans, F-
8 63000, Clermont-Ferrand, France.

9 ² *Instituto Geofísico Escuela Politécnica Nacional, Ladrón de Guevara E11-253 y Andalucía,*
10 *Quito, Ecuador.*

11 ³ *UCL Hazard Centre, Department of Earth Sciences, UCL, Gower St, London WC1E 6BT,*
12 *UK.*

13 ⁴ *Department of Space, Earth and Environment, Chalmers University of Technology,*
14 *Göteborg, Sweden.*

15 *Corresponding author. E-mail: j.battaglia@opgc.fr; tel: +33 473346779
16

17 **Abstract**

18 Eruption style and dynamics are controlled by various parameters including magma supply
19 rate, magma viscosity, volatile content, and the permeability of the conduit. Rapid changes of
20 these parameters can significantly modify the hazards associated to the eruption processes and
21 understanding their relationship with multiparametric geophysical monitoring data can greatly

22 improve our forecasting capacities. From 2008 to 2016, volcanic activity at Tungurahua was
23 characterized by eruptive phases separated by episodes of quiescence. These phases displayed
24 great variability of eruptive patterns including Vulcanian and Strombolian explosions, low
25 pyroclastic fountaining, continuous or sporadic ash emissions and passive degassing. We use
26 the comparison between geophysical data (seismic, acoustic and SO₂ emission), recorded by
27 permanent monitoring networks, and the characteristics of the emitted ash to track changes in
28 eruption dynamics during an eruptive phase that lasted from late December 2009 to March
29 2010. We show that the correlation between the analyzed parameters allows imaging and
30 interpretation of the conditions at the vent. At Tungurahua, these conditions can rapidly
31 change at the time scale of a single eruptive phase, corresponding to various degrees of
32 opening, plugging and permeability of the conduit. Two magma intrusions could be identified
33 during a single eruptive phase showing transitions between violent Strombolian and
34 Vulcanian activity. Changes in the componentry of the analyzed ash samples, together with
35 the geophysical data, nicely highlight these evolutions. Studying these parameters
36 simultaneously provides a unique insight into the physical processes controlling superficial
37 volcanic activity and offers a potential tool for better understanding volcanoes and detecting
38 changes in their activity. The joint interpretation of multiparametric data which we propose is
39 potentially applicable to multiple andesitic volcanoes.

40

41 **1. Introduction**

42 Stratovolcanoes with long-lasting eruptive cycles, such as Tungurahua (Ecuador), Sakurajima
43 (Japan), Semeru (Indonesia), Soufrière Hills (West Indies, United Kingdom) or Popocatepetl
44 (Mexico), among others, pose a significant threat to local populations for three main reasons.

45 1) They constantly expose local populations to variable amounts of ash that can create chronic
46 health diseases (Baxter et al., 2014) and have long-term impacts on livelihoods (Few et al.,
47 2017). 2) Continuous accumulation of pyroclastic material on the flanks of the volcanic
48 edifice promotes the formation of rain-triggered lahars (Jones et al., 2015). 3) Local
49 authorities and populations are used to the more frequent low activity of the volcano and
50 might underestimate or overrule the potential impacts of the less frequent larger eruptions
51 (Mothes et al., 2015). A recent example is the June 2018 eruption of Fuego volcano
52 (Guatemala) that caused the death of at least 198 people (INACIF, 2019). During long-lasting
53 eruptions, the eruptive dynamics can rapidly shift from low explosive activity to high
54 explosive activity that translates into a substantial increase of the volcanic threat (Hidalgo et
55 al., 2015). These variations in surface activity are typically controlled by the characteristics of
56 the magma, such as composition, viscosity, permeability, bubble and crystal contents
57 (Cashman and McConnell, 2005; Melnik et al., 2005; Heap et al., 2015), the conditions at the
58 vent (i.e. open or closed) (Diller et al., 2006), the geometry of the conduit (Vitturi et al., 2008)
59 and the magma discharge rate (Cassidy et al., 2015; Bonadonna et al., 2016). Some of these
60 parameters can be quantitatively determined afterwards by conducting a precise analysis of
61 volcanic products like pyroclasts and/or lava (Wright et al., 2012; Gurioli et al., 2015).
62 However, the combined analysis of continuous geophysical signals permanently recorded by
63 multiparametric monitoring networks can give, in near real-time, at least qualitative insights
64 into the volcano behavior and help to forecast eruptive events (Ripepe et al., 2002, 2005).
65 Accurately imaging the evolution of eruptive dynamics through geophysical observations
66 ideally requires multiparametric monitoring systems including seismic, acoustic, geodetic,
67 thermal, geochemical, IR measurements, and visual observations.

69 Tungurahua (5023 m a.s.l.) is an andesitic stratovolcano located in Central Ecuador. It has an
70 eruptive recurrence interval of 80-90 years (Le Pennec et al., 2008). The most recent eruptive
71 cycle started in September 1999 and lasted until March 2016, with a major VEI3 paroxysm in
72 August 2006 (Eychenne et al., 2012). Tungurahua, as many other andesitic volcanoes,
73 displays various types of eruption styles: continuous to sporadic gas and ash emissions,
74 individual explosions with ejecta of blocks, low pyroclastic fountaining, violent explosions
75 producing pyroclastic density currents, and lava flows (Arellano et al., 2008; Samaniego et
76 al., 2011; Eychenne et al., 2012; Hall et al., 2015; Hidalgo et al., 2015). Pyroclastic
77 fountaining (e.g. Branney and Kokelaar, 2002) is different from spattering or lava fountaining
78 given that the pyroclasts are already solid in the gas jet. This term is more appropriate to
79 describe the activity at Tungurahua, as pointed out by Bernard (2018). There is an extensive
80 literature on Tungurahua's recent eruptive cycle focused on seismo-acoustic activity (Johnson
81 et al., 2005; Kumagai et al., 2010; Kim et al., 2014; Bell et al., 2017), degassing (Arellano et
82 al., 2008; Hidalgo et al., 2015), ground deformation (Champenois et al., 2014; Neuberg et al.,
83 2018), and eruption products (Samaniego et al., 2011; Wright et al., 2012; Eychenne et al.,
84 2012; Douillet et al., 2013; Eychenne et al., 2013; Hall et al., 2015; Bernard et al., 2016).
85 However, none of this research uses more than two methods to characterize the activity.
86 Furthermore, this literature is mostly focused on large events, such as the 2006 eruption, or
87 long periods of activity. Smaller events ($VEI \leq 2$) are mostly neglected. This last comment can
88 also apply in general to most of literature in volcanology.

89

90 For this study, we use seismic, acoustic, and SO₂ emission data to characterize the eruption
91 mechanisms during a phase of eruptive activity, which occurred from December 2009 to
92 March 2010. During this phase, Tungurahua exhibited a wide range of eruptive processes

93 including passive degassing, continuous ash venting and transient volcanic Strombolian and
94 Vulcanian explosions. We compare geophysical parameters with visual observations of the
95 surface activity reported by the Instituto Geofísico of Escuela Politécnica Nacional (IG-EPN)
96 and with diverse characteristics (geochemistry, mineralogy, componentry and grain-size
97 distribution) of ash samples collected throughout this eruptive phase. We use these
98 comparisons to propose a model of the temporal evolution of the eruption and determine the
99 vent conditions. The correlations highlighted in this paper can be used to follow and forecast
100 rapid changes in eruptive dynamics at andesitic volcanoes that show transitions between
101 emissive and explosive behaviors.

102

103 **2. Quantification of geophysical parameters and ash characterization**

104 **2.1 Seismic, acoustic and SO₂ emission quantification**

105 Tungurahua is monitored by the IG-EPN whose monitoring network includes five short-
106 period and five broadband seismic stations coupled with acoustic sensors (Kumagai et al.,
107 2010), and three permanent scanning-DOAS instruments (Novac-I, Galle et al., 2010). The
108 location of these instruments is shown in Figure 1. We examined the seismic, acoustic and
109 SO₂ data recorded during the eruptive sequence, which started on December 30, 2009 and
110 lasted until March 4, 2010. The seismicity of Tungurahua includes a great variety of signals
111 related to eruptive activity including explosion quakes generated by individual explosions but
112 also various types of tremors and chugging signals related to longer-duration venting (Figure
113 2). To quantify both short- and long-term variations we proceeded in two ways.

114

115 We first quantified the acoustic and seismic energies of large individual explosions. For this
116 purpose, we used data from the broadband and acoustic sensors. For each explosion with an

117 acoustic peak-to-peak amplitude greater than 45 Pa at reference station BMAS located 5.5 km
118 from the summit (equivalent to 100 Pa at 1 km from the vent as mentioned by Hidalgo et al.,
119 2015), we calculated the seismic and acoustic energies at each station using the formulas
120 proposed by Johnson and Aster (2005), namely:

121

$$122 \quad E_{\text{acoustic}} = \frac{2\pi r^2}{\rho_{\text{atmos}} c_{\text{atmos}}} \int \Delta P(t)^2 dt \quad (1)$$

123

124 where E_{acoustic} is the acoustic energy (J), r is the distance from the station to the vent (between
125 4695 and 6341 m depending on station), ρ_{atmos} is the atmospheric density (between 0.7278 and
126 0.7878 kg/m³), c_{atmos} is the typical infrasound wave velocity at the average elevation of the
127 stations (339.2 m/s), $\Delta P(t)$ is the excess acoustic pressure measured by the instrument. And:

128

$$129 \quad E_{\text{seismic}} = 2\pi r^2 \rho_{\text{earth}} c_{\text{earth}} \frac{1}{A} \int S^2 U(t)^2 dt \quad (2)$$

130

131 where E_{seismic} is the seismic energy (J), ρ_{earth} is the volcano density (2380 kg/m³), c_{earth} is the
132 P-wave velocity (3500 m/s), A is the attenuation factor (between 0.7963 and 0.8305), S is the
133 site response (1 for all stations), $U(t)$ is the particle velocity (m/s) measured by the
134 seismometer.

135

136 For each event, average seismic and acoustic energies were estimated by taking the mean
137 value of respective energies calculated at the four less noisy stations (BMAS, BPAT, BRUN

138 and BBIL, see Figure 1), assuming a fixed location at the vent surface for all explosion
139 sources. Energies were then summed up on a daily basis to obtain cumulative seismic (SEE)
140 and acoustic (AEE) explosion energies. Calculations show that AEE is generally about 100
141 times higher than SEE and therefore, for comparison, we refer to a reference value of 100 for
142 the AEE/SEE ratio. A total of 521 explosions were identified based on these criteria. The
143 presence of these high-energy explosions allowed the distinction among High Explosive
144 Activity (HEA) and Low Explosive Activity (LEA) periods (Hidalgo et al., 2015).

145

146 To estimate the amplitude of longer-term processes such as tremor, we calculated median
147 seismic amplitudes (MSA) over 10-minute sliding windows for the full short-period
148 frequency range (0.5-25 Hz). To obtain the median value of each window, we filter the
149 seismic signal with a 4-pole Butterworth filter, calculate the absolute value of the seismic
150 amplitudes and determine the median value of the amplitude distribution. For this, we used
151 the short-period station RETU (Figure 1), because it is the closest (3900 m asl) to the summit
152 and better reflects surface activity compared to more distant stations. However, when the
153 station was either saturated or experiencing technical problems, the time-series was completed
154 by using data from station BMAS, after scaling its MSA by an empirical factor estimated to
155 guarantee the continuity of the recordings. This empirical factor was calculated by matching
156 the amplitudes at RETU and BMAS when both stations were working properly. In figure 3,
157 we present MSA as values integrated over one-day windows. Finally, to specifically quantify
158 monochromatic or harmonic tremor we used the IG-EPN catalog, which characterizes this
159 type of activity by estimating the duration and mean amplitude of each burst identified by
160 frequency analysis. We calculated for each burst the product of these two parameters and
161 summed them on a daily basis. Because of differences in the calculation mode, results from

162 the quantification of monochromatic/harmonic tremor cannot directly be compared with the
163 daily cumulative MSA.

164

165 Scanning-DOAS instruments provide SO₂ emission rate measurements only during typically
166 ten hours of daylight at the volcano location and under good weather conditions, leading to
167 sometimes sparse time-series. To quantify the daily SO₂ emission with data from a dense
168 DOAS monitoring network, Hidalgo et al. (2015) proposed integrating the highest validated
169 SO₂ emission rate measurements among all stations to obtain a *daily observed mass of SO₂*,
170 rather than extrapolating the highest of the averages calculated for each station over the
171 available measurements obtained during the day. The daily-observed mass is originally
172 expressed in tons per 10 hours (the constant daily measurement duration), but can easily be
173 expressed in tons per day (t/d) by multiplying by a factor 2.4. This approach better takes into
174 account the daily-validated measurement duration (DVMD), i.e. the time of effective
175 detection of gas, which is usually high during eruptive phases and low during quiescence.
176 This method significantly improves long-term (i.e. yearly) correlation between SO₂ emission
177 and eruptive activity, as demonstrated by Hidalgo et al. (2015).

178

179 **2.2 Ash characterization**

180 The geophysical datasets were completed with direct observations on the eruptive dynamics
181 compiled by the Tungurahua Volcano Observatory (OVT for the Spanish acronym). We also
182 derived different characteristics from a total of eight samples of ash deposits collected by
183 volunteers on solar panels located at 6 to 8 km distance from the vent, on the WSW flank of
184 the volcano (under the most common wind direction) during the studied eruptive period.

185 These characteristics are: 1) bulk ash chemistry of major elements, 2) semi-quantitative
186 mineralogy, 3) componentry, and 4) grain-size distribution.

187

188 Bulk ash chemistry and semi-quantitative mineralogy were obtained at the Departamento de
189 Metalurgia Extractiva of the Escuela Politécnica Nacional (DEMEX-EPN). For the chemical
190 analysis we used an S8 TIGER High-end wavelength-dispersive X-ray fluorescence
191 (WDXRF) spectrometer with Spectra plus software. Analytical errors are around 1%. Semi-
192 quantitative mineralogy was obtained through X-ray diffraction (D8 Advance and Diffrac plus
193 software). Manual sieving and componentry were performed at the IG-EPN. The
194 componentry analysis followed the methodology described by Eychenne et al. (2012, 2013).
195 Over 300 grains were classified through optical microscopy and Secondary Electron
196 Microscopy (SEM) from at least four grain-size classes for each sample. Grain-size
197 distribution was obtained combining manual sieving for coarse fractions (-2 to 4ϕ or D
198 between 16 and 0.063 mm, with $\phi = -\log_2 D$ where D is the particle diameter in mm) and laser
199 diffraction (Horiba LA-9520V2) for the fine fractions ($>4 \phi$ or $D < 0.063$ mm).

200

201 Bulk ash samples showed a homogenous andesitic composition throughout the two months of
202 eruption ($\text{SiO}_2 = 57.81 \pm 0.22\%$, $\text{K}_2\text{O} = 1.73 \pm 0.04\%$; 6 samples). Mineralogical assemblage
203 was characterized by plagioclase, clinopyroxene, orthopyroxene, olivine, and magnetite. This
204 assemblage was also constant for the 6 analyzed samples (Plagioclase = $61.0 \pm 0.9\%$;
205 Clinopyroxene = $32.7 \pm 1.9\%$; Orthopyroxene = $4.8 \pm 1\%$; Olivine = $1.3 \pm 0.5\%$; Magnetite =
206 $0.2 \pm 0.4\%$). These results are in agreement with previous analyses reported by Samaniego et
207 al. (2011).

208

209 Componentry analysis allowed the identification of eight classes (Figure 4). Four classes were
210 formed by juvenile material, two classes displayed accidental components, one comprised
211 only free crystals and the last class showed both juvenile and accidental features. Juvenile
212 components were identified as material exhibiting fresh vitreous shiny surface. They were
213 then divided according to their color (dark or honey) and vesicularity (dense or scoriaceous).
214 Accidental components were identified as material exhibiting more matte or opaque surfaces.
215 There were two accidental classes: 1) accidental oxidized fragments that showed a
216 homogeneous and penetrating reddish color, and 2) grey lithics that were generally dense and
217 slightly altered. Free crystals without attached groundmass were counted apart as it was
218 impossible to determine their origin with optical microscopy. Finally, an important class was
219 the vitreous oxidized fragments that exhibited both juvenile and accidental features. They
220 presented a very thin layer of rust on top of a shiny surface. This material was interpreted as
221 recycling of slightly altered, mostly fresh, material from the active crater (Acuña, 2017).
222 Significant variations were observed in the componentry (eight samples) throughout this
223 phase, with the beginning being characterized by honey color of mostly vesicular juvenile
224 material evolving through time to dark color of mostly dense juveniles. The detailed evolution
225 will be described in the next section together with the observed seismic and degassing
226 changes.

227

228 Grain-size distribution (six samples) was characterized by very fine to extremely fine ash (Mz
229 = $3.38-4.52 \phi$; $\sigma = 1.75-2.43 \phi$; with $Mz = \text{mean } ((\phi_{16} + \phi_{50} + \phi_{84})/3)$ and $\sigma = \text{standard}$
230 $\text{deviation } ((\phi_{84} - \phi_{16})/4 + (\phi_{95} - \phi_5)/6)$ as defined in Folk and Ward, 1957) and showed some
231 changes during this eruptive phase. All the samples showed bimodal distributions, with a

232 coarse mode between 1.8 and 2.9 ϕ (medium to fine ash), and a fine mode between 5.9 and
233 6.4 ϕ (extremely fine ash). In general, we observed coarsening of the coarse mode while the
234 fine mode remained rather constant throughout the eruption.

235

236 The ash data set does not mimic exactly the geophysical data because the ash samples were
237 both discontinuous and accumulated over inconsistent periods of time (few days to about a
238 week). This sampling creates an artificial smoothing of the changes in eruptive dynamics.
239 This is why in general geophysical data allow to better identify the different episodes but we
240 argue that petrological monitoring adds significant information to the conventional
241 geophysical monitoring and allows to better constrain the conduit processes (Gaunt et al.,
242 2016).

243

244 **3. Chronology of the eruptive phase**

245 The eruptive phase from December 2009 to March 2010 followed a period of almost six
246 months of quiescence. During this quiescent period, no surface activity was visually observed.
247 To describe eruptive activity at Tungurahua, Hidalgo et al. (2015) distinguished between LEA
248 (yellow background color in Figure 3) and HEA periods (orange in Figure 3). These last
249 periods are characterized by discrete, high-amplitude explosions, for which we have
250 calculated explosion energies (SEE and AEE), as described above. The eruptive phase
251 discussed here includes two periods of LEA separated by one period of HEA. We divide the
252 eruptive phase into six episodes whose beginning and end were defined according to changes
253 in the temporal evolutions of the geophysical parameters described above (Figure 3). The
254 evolution of componentry and grain-size of the ash is shown in Figure 4 and detailed for each
255 episode.

256

257 (a) *30 December 2009 – 3 January 2010: seismically silent magma ascent and degassing.* The
258 first signs of eruptive activity were observed late on 30 December 2009 with the occurrence
259 of a long period (LP) event followed by the emission of a small gas plume that reached a
260 height of ~300 m above the crater. A steady SO₂ emission rate (967 ± 221 t/d) was measured
261 during the following three days, with very small ash emission up to 1.5 km above the summit
262 (not seen by satellite instruments), accompanied by weak roaring sounds. This episode was
263 characterized by the almost complete absence of seismicity, even at station RETU, the closest
264 to the summit (2 km), except for a few small amplitude LP events. Despite this quiet onset,
265 visual observations inside the crater on 2 January indicated the presence of an incandescent
266 lava accumulation in the actively degassing crater. This feature was absent in November 2009.
267 This activity did not produce a significant amount of ash, leading only to very thin fallouts
268 restricted to the crater area. This prevented any ash sampling for this episode. The activity
269 began to change on 3 January with SO₂ emission increasing up to 3400 t/d.

270

271 (b) *3 - 10 January 2010: appearance of tremor.* After four days of degassing and weak ash
272 emissions, seismic signals related to venting processes appeared simultaneously with semi-
273 continuous ash plumes reaching up to 4.1 km above the crater (as reported by the Washington
274 VAAC) and weak pyroclastic fountaining. Few discrete explosions were recorded during this
275 episode. A progressive buildup of the MSA accompanied an irregular increase and
276 stabilization of SO₂ emissions, which averaged 3073 ± 1140 t/d during the episode. SO₂
277 individual measurements showed an increase in daily variability, indicating a more
278 discontinuous gas discharge, which is in agreement with the appearance of tremor pulses that
279 occasionally had large amplitudes (MSA peak on 7 January). Episodes of harmonic tremor

280 started on 7 January. This activity was associated with low-to-moderate intensity roaring
281 sound. During this episode the ash grain-size distribution was bimodal and fine-grained, as for
282 most of the eruption. Ash componentry was dominated (>85 %) by honey-color juvenile
283 fragments (mostly scoria), with some free crystals and a very small amount of accidental
284 material (grey lithics or oxidized fragments) and dark-color juvenile (two samples 06/01 in
285 Figure 4).

286

287 (c) *11 - 15 January 2010: appearance of larger explosions.* On 11 January, a major change
288 was observed in eruptive activity with the appearance of larger explosions with typical canon-
289 like shot sounds, sometimes followed by high amplitude tremor. This transition was not
290 accompanied by any marked increase in the flux of SO₂, which remained stable around 2760
291 ± 1516 t/d. This highly explosive activity, which lasted for five days, showed strong seismic
292 energy partitioning (AEE/SEE<<100). The superficial activity was characterized by
293 explosions ejecting ballistics, followed by low pyroclastic fountaining. This activity was
294 associated with sustained ash plumes (typically 3 km-high, and up to 5 km-high) and
295 moderate-to-high intensity roaring sound. Harmonic tremor was recorded throughout the
296 episode and almost vanished afterwards (Figure 3). Moderate to strong ash fallouts occurred
297 during this episode. The change of eruptive activity was directly recorded in the componentry
298 of the ash sample while the grain-size distribution remained unchanged and fine-grained
299 (sample 12/01). The amount of honey-color juvenile material dropped to ~37% while the
300 amount of dark-color and vitreous oxidized particles rose to 34 and 20% respectively. Free
301 crystals and grey lithics remained very scarce (Figure 4).

302

303 (d) *16 - 23 January 2010: drop of explosive activity.* A drop in explosive activity (SEE and
304 AEE) was observed on 16 January coinciding with a decrease and stabilization of tremor
305 amplitude as seen in the MSA. A few less energetic explosions remained with a ratio
306 AEE/SEE>100. This drop in seismicity was, however, only accompanied by a very small
307 reduction of SO₂ emissions (2495 ± 887 t/d). Pyroclastic fountaining and quasi-continuous
308 gas and ash emissions reaching up to 3 km above the summit were observed, associated with
309 moderate intensity roaring sounds and small-to-moderate intensity ash fallouts, whose
310 juvenile fraction was dominated by dark-color and scoriaceous material (sample 20/01).

311

312 (e) *24 January - 24 February 2010: increase in larger explosions.* Large explosions resumed
313 progressively from 24 January with an energy increasing irregularly until 11 February before
314 decaying towards the end of the episode. This change was correlated with an intensification of
315 roaring and canon-shot-like sounds, an increase of column height (typically 2 km and up to 4
316 km above the summit) and ash content of the emissions. Compared to episode (c), the daily
317 number of large explosions was similar but the SEE was significantly lower and the AEE
318 higher, resulting in a ratio AEE/SEE>100 during most of the episode, similarly to episode (d).
319 A decrease of this ratio (<100) was observed during the end of the episode, simultaneously
320 with the drop of both energies. Accompanying this activity, the MSA decreased smoothly
321 except for a short increase peaking around 5 February. These signals corresponded to a
322 progressive decrease of background tremor, which was replaced by occasional LPs or
323 explosions. Grain-size distribution showed a significant increase in the fine mode fraction
324 compared to previous episodes (Sample 6/02). During this episode, the SO₂ emission
325 displayed significant fluctuations with a globally decaying trend (1729 ± 1272 t/d), except for
326 a short-duration increase roughly synchronous with the one observed for the MSA and the

327 change in grain-size distribution (Sample 6/02). Small pyroclastic flows due to collapses of
328 the material accumulated near the vent occurred at the end of this episode. This was followed
329 by a slight coarsening of the ash grain-size. The ash componentry became clearly dominated
330 (>85 %) by dark-color juvenile fragments (samples 17 and 24/02). Also, interestingly, we
331 observed an increase of dense material compared to scoria.

332

333 (f) *25 February to 4 March 2010: dying out of the activity.* By 25 February, sporadic ash
334 emissions (less than 3 km-high) were observed with only minor seismic activity: a few
335 transient events including mostly LPs and no significant tremor. SO₂ was almost at
336 background levels observed during quiescence periods (78 ± 41 t/d). The small ash fallouts
337 during this episode showed a slight decrease of the amount of dark-color juvenile material
338 even though it still remained as the main component (>80%). The ash grain-size distribution
339 was also slightly finer-grained compared to the episode (e) mostly associated to a higher
340 amount of the fine sub-population mode (sample 07/03).

341

342 The average emission rate of SO₂ during the entire eruptive phase was 1807 ± 1394 t/d, which
343 is equivalent to a total gas release of about 120 kt of SO₂ to the atmosphere during the 65 days
344 of activity. We found average emissions of 2020 ± 1302 during HEA (45 days) and $1430 \pm$
345 1591 t/d during LEA (20 days). It could be argued that this difference reflects a real change in
346 gas emissions. A t'Student test of the difference between the averages of the two samples
347 (HEA and LEA daily measurements) resulted in a p-value of 0.08, meaning an 8% probability
348 of having observed a false difference by chance. However, we note that the size of our
349 samples is not large enough to derive a robust conclusion in a statistically significant sense.

350 The typical uncertainty of individual measurements is estimated at about 30% (see Galle et
351 al., 2010; Hidalgo et al., 2015).

352

353 **4. Discussion**

354 The comparison of the different geophysical time series with visual observations of
355 superficial activity and ash characteristics provides unique information about the eruptive
356 dynamics and processes occurring in the conduit. We discuss and interpret the parameters for
357 each episode to recompose the temporal evolution of the eruptive phase. The sketches shown
358 in Figure 5 illustrate this evolution.

359

360 *(a) Open conduit, silent magmatic ascent with free magma degassing*

361 The progressive and seismically silent appearance of gas during episode (a) can be interpreted
362 as a new batch of magma reaching the surface through an open conduit, with SO₂ easily and
363 rapidly exsolving through a permeable ascending magmatic column. This corresponds to the
364 seemingly seismically silent emplacement of the lava observed in the crater on 2 January. This
365 lack of seismicity is rather uncommon, especially for magmas with a high viscosity. For
366 basaltic magmas, seismically silent lava outpouring from a shallow pocket has been reported
367 at Etna (Bonaccorso et al., 2006), and Eibl et al. (2017) reported silent magma transport at
368 Bardarbunga after dyke opening. At Tungurahua, the high temperature (~1000°C) of andesites
369 (58-59 wt.% SiO₂) and their high water content (5-6 wt.% H₂O) may result in a relatively low
370 viscosity magma (Samaniego et al., 2011; Andújar et al., 2017). Therefore, the slow
371 emplacement of a small volume of lava in the crater, originating from a shallow source, as
372 well as the fact that the closest station is located at about 2 km from the crater, could explain
373 the absence of recorded seismicity. The low ash content in the emissions was likely due to

374 passive reworking of ash driven by high gas pressure (Figure 5a). Our observations suggest
375 that when the conduit is open to magma transport, a seismically silent propagation of magma
376 is possible but not without generating SO₂ emission.

377

378 *(b) Removal of the blocky lava surface and deepening of the fragmentation surface*

379 The sustained degassing and low explosive activity may have resulted in the removal of part
380 of the blocky lava emplaced at the top of the conduit toward the end of episode (a). Such a
381 process may have lowered the pressure in the conduit, leading to an increase in the amount of
382 exsolved SO₂ as observed since 3 January. This type of depressurization-induced degassing
383 has been modeled by Girona et al. (2014). Higher gas exsolution could have led in turn to
384 magmatic fragmentation, which would have progressively depleted the upper part of the
385 magma column. This process would result in an increase in viscosity and density of the
386 remaining magma, ultimately generating a denser, less fluid and permeable zone in the
387 magma column. This is in agreement with the model proposed by Diller et al. (2006) based on
388 the 1997 Vulcanian activity of Soufrière Hills volcano, Montserrat. The progressive
389 appearance of tremor during episode (b) is in good agreement with the formation of a
390 rheological barrier or partial plug. Tremor or tremor bursts may be caused by resonances
391 induced in this barrier by the continuous or intermittent transit of gas through this denser
392 zone, based on similar mechanisms to those proposed by Ferrick et al. (1982) or Julian et al.
393 (1994) for the generation of tremor, for example. Preliminary locations obtained for eruptive
394 phases in 2014 with a dense seismic network (Battaglia et al., 2015), suggest that a large part
395 of volcanic sources (tremors, LPs, explosion quakes) may be located about 1 km below the
396 summit. This depth is in agreement with results found by Kumagai et al. (2010) and Kim et al.
397 (2014) for explosion sources at Tungurahua recorded respectively in May 2009 and May

398 2010. Since the source location appears to be relatively constant through time, we may
399 speculate that the barrier at the origin of tremors and explosions during our eruptive phase
400 was formed at about 1 km below the summit (800 m below the crater floor). The increase of
401 tremor amplitude may be related to the progressive narrowing of the resonating conduit or an
402 increase in gas flux and ash emissions. The occurrence of harmonic tremor during this episode
403 may be explained by specific geometries of the conduit during the formation of the dense
404 barrier, leading to specific dominant frequencies in a similar way to the clarinet model
405 proposed by Lesage et al. (2006) for Arenal volcano. The shallow activity (violent
406 Strombolian explosions, low pyroclastic fountaining and small ash plumes) might be
407 explained by the migration of volatiles through the low-viscosity magma in the upper part of
408 the conduit, leading to magmatic fragmentation and enhancing the growth of the plug. The
409 mostly vesiculated honey-color juvenile material would be the evidence of this shallow
410 magmatic fragmentation and rapid ascent of magma through the conduit. Similar vesicular
411 material has been observed at Villarrica volcano and reported as golden pumice by Gurioli et
412 al. (2008).

413

414 *(c) Explosive activity during conduit cleaning, muffling effect and stiffening of the rheological barrier*

415 The appearance of large explosions during episode (c), without any large increase in the rate
416 of SO₂ degassing, suggests a transition in the way in which gas escapes rather than an increase
417 in the amount of exsolved gas. The barrier formed during episode (b) acts like a plug or valve
418 system during episode (c), leading to the accumulation and cyclic release of highly over-
419 pressured gases that trigger Vulcanian explosions. A similar mechanism is proposed by
420 Campion et al. (2018) for E2-type explosions at Popocatepetl volcano. Nevertheless, in this
421 last case the gas is unable to escape due to a rapid gravitational compaction of dome, while

422 we propose a densification of the magma due to the exsolution and loss of gas following the
423 model of Heap et al. (2015). Magma densification by gas loss and conduit plug formation
424 have also been modeled by Diller et al. (2006) and used to explain Vulcanian activity at
425 Soufrière Hills. These authors showed that a dense zone, a plug, could be produced at 750 m
426 depth, a depth similar to the one assumed in present work (800 m below the crater level).
427 During episode (c), the plug sits below already fragmented juvenile and old material, which
428 results in a muffling of acoustic waves and a ratio $AEE/SEE \ll 100$. Recycling of this material
429 in the ash column is evidenced by the drastic increase of vitreous oxidized material in the ash
430 componentry. Large explosions eject parts of this material as well as new magmatic foam and
431 gases released through the plug. Dark juvenile material shows a sharp increase at this time.
432 Similar dark dense material has also been reported in direct relation to Vulcanian explosions
433 at Colima volcano (Cassidy et al., 2015). Harmonic tremor is still generated, sometimes
434 following the occurrence of large explosions, and might be associated to the production of
435 honey-color juvenile material. These internal processes coincide with the strongest superficial
436 activity interpreted as a mixed dynamism between violent Strombolian, mainly characterized
437 by the dominance of honey-color juvenile components, and Vulcanian eruptive styles,
438 dominated by dark juveniles.

439

440 *(d) Open conduit and triggering of a second magmatic pulse*

441 After the partial or complete destruction of the plug, the conduit is partially open again during
442 episode (d). The pressure drop produced by the partial emptying of the conduit might have
443 triggered a new magmatic injection through a depressurization mechanism similar to that
444 proposed by Girona et al. (2014). The absence of chemical or mineralogical changes in the
445 subsequent eruptive products suggests that the source of this new injection is the same as the

446 one that occurred during episode (a). According to Samaniego et al. (2011), the magmatic
447 reservoir that fed the shallow system between 1999 and 2006 was located between 7.5 and 9.5
448 km below the summit. This arrival of new magma explains the sustained SO₂ degassing and
449 ash venting observed despite the clear decrease of superficial activity at the end of episode
450 (c). Mostly continuous tremor is recorded accompanying these SO₂ and ash emissions.
451 Starting with this episode, the smoothed SO₂ time-series roughly follows the MSA,
452 suggesting a common source process. Only a few significant explosions are observed which
453 may relate to the occasional formation of an impermeable zone near the free surface, as
454 supported by the AEE/SEE ratio (>100). Dark-color and honey-color juvenile material are
455 fairly equivalent during this episode.

456

457 *(e) Explosive events after conduit cleaning, followed by progressive stiffening of the plug*
458 *inside the conduit*

459 Episode (e) shows a new increase in the number of significant explosions, except that a high
460 AEE/SEE ratio (>100) is recorded during most of the episode, suggesting that the upper
461 conduit is less clogged in comparison to episodes b and c. In terms of magma supply, it can be
462 interpreted as composed of two sub-episodes, from 24 January to 4 February (e.i), and from 5
463 to 24 February (e.ii), repeating a waxing-waning sequence similar to the one which occurred
464 during episodes (b), (c) and (d). Therefore, (e.i) is interpreted as the increase of activity
465 caused by the arrival of new gas-rich magma. However, compared to (b), the presence of a
466 more efficient rheological barrier (plug) or a deeper level of fragmentation may explain the
467 occurrence of Vulcanian explosions in between of the dominating violent Strombolian activity
468 (Bernard, 2018). In contrast, (e.ii) would rather correspond to waning of the episode with
469 more “pure” Vulcanian activity, as shown by the seismo-acoustic ratios of explosions and the

470 clear increase in dense black juvenile components in the ash and the coarsening of the grain-
471 size dominant mode. The decrease in SO₂ emissions, explosion energies and MSA during
472 (e.ii) indicates a decreasing magma supply rate. This would lead to the progressive plugging
473 and obstruction of the conduit. Its progressive burial may then explain the decrease of the
474 AEE/SEE ratio (<100) observed toward the end of the episode.

475

476 (f) *Sealing of the system*

477 Finally, episode (f) corresponds to the final closing and sealing of the conduit with only
478 residual ash and gas being emitted. The characteristics of the ash are similar to those from
479 episode (e) with a small increase of oxidized material, recycled from the vent. The plug
480 emplaced at the end of the eruption was later broken at the beginning of the following
481 eruptive phase which started in May 2010 with Vulcanian explosions and moderate-size
482 pyroclastic flows (Kim et al., 2014; Hidalgo et al., 2015; Bernard, 2018).

483

484 The eruptive phase that we studied, displayed a wide spectrum of eruptive dynamics. We
485 interpret this diversity as being the result of variable conditions of opening or constriction of a
486 rheological barrier or plug in the conduit, additionally to variations in the magma supply rate.
487 Despite the morphological differences, Soufrière Hills volcano displayed similar dynamics
488 during its eruptive activity from 2005 to 2010, showing also ash venting and Vulcanian
489 explosions. At Soufrière Hills, Cole et al. (2014) explained the ash venting by short term
490 increases in the extrusion rate related to shear-induced fragmentation at the conduit margin.
491 Seismic tremor and ash componentry were similar to what we observed in episode (b). The
492 origin of Vulcanian explosions at Popocatepetl or Montserrat is ascribed respectively to the
493 self-collapse of the dome (Campion et al., 2018) and the sealing of the dome cracks, allowing

494 degassing, by precipitation of hydrothermal minerals (Edmonds et al., 2003). At Tungurahua,
495 the activity does not include the formation of domes and its Vulcanian explosions are more
496 similar to those observed at Sakurajima volcano (Watt et al., 2007). Hence, we argue that a
497 high-viscosity, high-density barrier inside the conduit is responsible for the occurrence of
498 Vulcanian explosions, following the experimental models proposed by Heap et al.
499 (2015), while the violent Strombolian activity is probably associated to a hotter less
500 degassed magma.

501

502 **5. Conclusions**

503 The comparison of seismic, acoustic and SO₂ gas emission time series recorded during the
504 December 2009 - March 2010 eruptive phase of Tungurahua volcano outlines diverse patterns
505 and correlations between the parameters. Based on this diversity, we identified 6 episodes
506 with different characteristics, which we interpret in terms of conduit conditions and magma
507 supply rate. During these episodes, degassing could freely occur without generating any
508 seismicity if the conduit was open. Tremor could be observed, including monochromatic
509 tremor if the conduit was (properly) constricted and larger Vulcanian explosions could occur
510 if it was occasionally or partially plugged. At some point, dynamics changed from continuous
511 degassing during ash venting and violent Strombolian activity to a degassing dominated by
512 Vulcanian explosions without any significant change in the amount of SO₂ emitted from the
513 vent.

514

515 We associate this variability to changes in the conduit and more specifically to the evolution
516 of a rheological barrier or plug which we assume to be about 1 km below the summit based on
517 locations of seismic sources. Vent conditions and fragmentation processes are also clearly

518 reflected in the ash componentry and to a lower degree in the grain-size distribution. Our
519 results suggest that the correlation of multiparametric data can highlight transitions in the
520 nature of superficial activity that can be confirmed through petrological monitoring. They also
521 outline geophysical patterns that allow to identify two waxing-waning cycles within the
522 eruptive phase produced by a second magmatic injection. The geophysical and petrological
523 signature of the two cycles was different as the conduit conditions evolved.

524

525 Comparing and correlating the different parameters allow making better interpretations of the
526 eruption evolution which is of major importance to improve hazard assessment. Our
527 interpretation patterns may be applied to most andesitic volcanoes independently of the
528 presence of plugs or domes which may act as shallow rheological barriers.

529

530 **ACKNOWLEDGEMENTS**

531 We are grateful to the staff of the IG-EPN for providing high quality data that made this work
532 possible. We thank also two anonymous reviewers and editor Tamsin Mather who helped to
533 greatly improve the manuscript. We are grateful to Andrew Harris for helpful comments. This
534 research has been conducted in the context of the Laboratoire Mixte International “Séismes et
535 Volcans dans les Andes du Nord” of IRD.

536

537 **WEB REFERENCES**

538 INACIF, [http://www.inacif.gob.gt/index.php/component/content/article/89-](http://www.inacif.gob.gt/index.php/component/content/article/89-noticias/ultimas-noticias/116-actualizacion-de-los-datos-del-trabajo-realizado-por-personal-del-inacif-en-atencion-a-la-emergencia-producida-por-la-erupcion-del-volcan-de-fuego)
539 [noticias/ultimas-noticias/116-actualizacion-de-los-datos-del-trabajo-realizado-por-personal-](http://www.inacif.gob.gt/index.php/component/content/article/89-noticias/ultimas-noticias/116-actualizacion-de-los-datos-del-trabajo-realizado-por-personal-del-inacif-en-atencion-a-la-emergencia-producida-por-la-erupcion-del-volcan-de-fuego)
540 [del-inacif-en-atencion-a-la-emergencia-producida-por-la-erupcion-del-volcan-de-fuego](http://www.inacif.gob.gt/index.php/component/content/article/89-noticias/ultimas-noticias/116-actualizacion-de-los-datos-del-trabajo-realizado-por-personal-del-inacif-en-atencion-a-la-emergencia-producida-por-la-erupcion-del-volcan-de-fuego)
541 (accessed 17/1/2019)

542

543 **BIBLIOGRAPHY**

544 Acuña Mondragón, K.E., 2017. Análisis de las cenizas del Tungurahua (granulométrico, de
545 componentes y químico) en la primera fase eruptiva de 2010 (enero-marzo). BSc Eng. project
546 thesis, Escuela Politécnica Nacional, Quito (Ecuador), 144 p.

547 Andújar, J., Martel, C., Pichavant, M., Samaniego, P., Scaillet, B., Molina, I., 2017.
548 Structure of the plumbing system at Tungurahua volcano, Ecuador: insights from phase
549 equilibrium experiments on July-August 2006 eruption products. *Journal of Petrology*, 58(7),
550 1249-1278, <https://doi.org/10.1093/petrology/egx054>.

551 Arellano, S.R., Hall, M., Samaniego, P., Le Pennec, J.-L., Ruiz, A., Molina, I., Yepes, H.,
552 2008. Degassing patterns of Tungurahua volcano (Ecuador) during the 1999–2006 eruptive
553 period, inferred from remote spectroscopic measurements of SO₂ emissions. *J. Volcanol.*
554 *Geotherm. Res.* 176(1), 151-162, <https://doi.org/10.1016/j.jvolgeores.2008.07.007>.

555 Battaglia, J., Hartmann, J., Hidalgo, S., Douchain, J.-M., Cordova, J., Alvarado, A., Ruiz,
556 M., Parra, R., 2015. Location and waveform classification of seismicity at Tungurahua
557 volcano (Ecuador) during the February and April 2014 eruptive phases. In 2015 AGU Fall
558 Meeting.

559 Baxter, P.J., Searl, A.S., Cowie, H.A., Jarvis, D., Horwell, C.J., 2014. Evaluating the
560 respiratory health risks of volcanic ash at the eruption of the Soufriere Hills Volcano,
561 Montserrat, 1995 to 2010. *Geological Society, London, Memoirs* 39(1), 407-425,
562 <https://doi.org/10.1144/M39.22>.

563 Bell, A. F., Hernandez, S., Gaunt, H. E., Mothes, P., Ruiz, M., Sierra, D., Aguaiza, S.,
564 2017. The rise and fall of periodic 'drumbeat' seismicity at Tungurahua volcano, Ecuador.
565 *Earth Planet. Sci. Lett.* 475, 58-70, <https://doi.org/10.1016/j.epsl.2017.07.030>.

566 Bernard, J., Eychenne, J., Le Pennec, J.-L., Narvaez Rivadeneira, D., 2016. Mass budget
567 partitioning during explosive eruptions: insights from the 2006 paroxysm of Tungurahua
568 volcano, Ecuador, *Geochem. Geophys. Geosyst.* 17, <https://doi.org/10.1002/2016GC006431>.

569 Bernard, B., 2018. Rapid hazard assessment of volcanic ballistic projectiles using long-
570 exposure photographs: insights from the 2010 eruptions at Tungurahua volcano, Ecuador.
571 *Volcanica* 1(1), 49-61. doi: <https://doi.org/10.30909/vol.01.01.4961>.

572 Bonaccorso, A., Bonforte, A., Guglielmino, F., Palano, M., Puglisi, G., 2006. Composite
573 ground deformation pattern forerunning the 2004–2005 Mount Etna eruption. *J. Geophys.*
574 *Res., Solid Earth* 111(B12), <https://doi.org/10.1029/2005JB004206>.

575 Bonadonna, C., Cioni, R., Costa, A. et al., 2016. MeMoVolc report on classification and
576 dynamics of volcanic explosive eruptions. *Bull. Volcanol.* 78(11), 84,
577 <https://doi.org/10.1007/s00445-016-1071-y>.

578 Branney, M.J., Kokelaar, B.P., 2002. *Pyroclastic Density Currents and the Sedimentation of*
579 *Ignimbrites*. Geological Society of London, 156 p. ISBN 978-1-86239-124-6.

580 Champion, R., Delgado-Granados, H., Legrand, D., Taquet, N., Boulesteix, T., Pedraza-
581 Espitía, S., Lecocq, T., 2018. Breathing and Coughing: The extraordinarily high degassing of
582 Popocatepetl volcano investigated with an SO₂ camera. *Frontiers in Earth Science* 6, 163,
583 <https://doi.org/10.3389/feart.2018.00163>.

584 Cashman, K.V., McConnell, S.M., 2005. Multiple levels of magma storage during the 1980
585 summer eruptions of Mount St. Helens, WA. *Bull. Volcanol.* 68, 57-75,
586 <https://doi.org/10.1007/s00445-005-0422-x>.

587 Cassidy, M., Cole, P.D., Hicks, K.E., Varley, N.R., Peters, N., Lerner, A.H., 2015. Rapid
588 and slow: Varying magma ascent rates as a mechanism for Vulcanian explosions. *Earth*
589 *Planet. Sci. Lett.* 420, 73-84, <https://doi.org/10.1016/j.epsl.2015.03.025>.

590 Champenois, J., Pinel, V., Baize, S., Audin, L., Jomard, H., Hooper, A., Alvarado, A.,
591 Yepes, H., 2014. Large-scale inflation of Tungurahua volcano (Ecuador) revealed by
592 Persistent Scatterers SAR interferometry. *Geophys. Res. Lett.* 41(16), 5821-5828,
593 <https://doi.org/10.1002/2014GL060956>.

594 Cole, P.D., Smith, P., Komorowski, J.-C., Alfano, F., Bonadonna, C., Stinton, A.,
595 Christopher, T., Odbert, H.M., Loughlin, S., 2014. Ash venting occurring both prior to and
596 during lava extrusion at Soufriere Hills Volcano, Montserrat, from 2005 to 2010. *Geological*
597 *Society, London, Memoirs*, 39(1), 71-92.

598 Diller, K., Clarke, A.B., Voight, B., Neri, A., 2006. Mechanisms of conduit plug formation:
599 Implications for vulcanian explosions, *Geophys. Res. Lett.* 33(20),
600 <https://doi.org/10.1029/2006GL027391>.

601 Douillet, G.A., Pacheco, D.A., Kueppers, U., Letort, J., Tsang-Hin-Sun, È., Bustillos, J.,
602 Hall, M., Ramón, P., Dingwell, D.B., 2013. Dune bedforms produced by dilute pyroclastic
603 density currents from the August 2006 eruption of Tungurahua volcano, Ecuador. *Bull.*
604 *Volcanol.* 75(11), 762, <https://doi.org/10.1007/s00445-013-0762-x>.

605 Edmonds, M., Oppenheimer, C., Pyle, D.M., Herd, R.A., Thompson, G., 2003. SO₂
606 emissions from Soufrière Hills Volcano and their relationship to conduit permeability,

607 hydrothermal interaction and degassing regime. *J. Volcanol. Geotherm. Res* 124(1-2), 23-43,
608 [https://doi.org/10.1016/S0377-0273\(03\)00041-6](https://doi.org/10.1016/S0377-0273(03)00041-6).

609 Eibl, E.P., Bean, C.J., Vogfjörð, K.S., Ying, Y., Lokmer, I., Möllhoff, M., O'Brien, G.S.,
610 Pálsson, F., 2017. Tremor-rich shallow dyke formation followed by silent magma flow at
611 Bárðarbunga in Iceland. *Nat. Geosci.* 10(4), 299, <https://doi.org/10.1038/ngeo2906>.

612 Eychenne, J., Le Pennec, J.-L., Troncoso, L., Gouhier, M., Nedelec J.-M., 2012. Causes
613 and consequences of bimodal grain-size distribution of tephra fall deposited during the August
614 2006 Tungurahua eruption (Ecuador). *Bull. Volcanol.* 74, 187-205.
615 <https://doi.org/10.1007/s00445-011-0517-5>.

616 Eychenne J., Le Pennec J.-L., Ramón P., Yepes H., 2013. Dynamics of explosive
617 paroxysms at open-vent andesitic systems: High-resolution mass distribution analyses of the
618 2006 Tungurahua fall deposit (Ecuador). *Earth Planet. Sci. Lett.* 361, 343–355,
619 <https://doi.org/10.1016/j.epsl.2012.11.002>.

620 Ferrick, M.G., Qamar, A., St. Lawrence, W.F., 1982. Source mechanism of volcanic tremor.
621 *J. Geophys. Res.* 87, 8675-8683.

622 Few, R., Armijos, M.T., Barclay, J., 2017. Living with Volcan Tungurahua: the dynamics of
623 vulnerability during prolonged volcanic activity. *Geoforum* 80, 72-81,
624 <https://doi.org/10.1016/j.geoforum.2017.01.006>.

625 Folk, R.L., Ward, W.C., 1957. Brazos river bar (Texas): a study of the significance of
626 grain-size parameters. *J Sediment Petrol* 27(1), 3-26.

627 Galle, B., Johansson, M., Rivera, C., Zhang, Y., Kihlman, M., Kern, C., Lehmann, T., Platt,
628 U., Arellano, S., Hidalgo, S., 2010. Network for Observation of Volcanic and Atmospheric
629 Change (NOVAC) - a global network for volcanic gas monitoring: network layout and

630 instrument description. *J. Geophys. Res., Atmos* 115(D5), 2156–2202,
631 <https://doi.org/10.1029/2009JD011823>.

632 Gaunt, H.E., Bernard, B., Hidalgo, S., Proaño, A., Wright, H., Mothes, P., Criollo, E.,
633 Kueppers, U., 2016. Juvenile magma recognition and eruptive dynamics inferred from the
634 analysis of ash time series: The 2015 reawakening of Cotopaxi volcano. *J. Volcanol.*
635 *Geotherm. Res.* 328, 134-146, <https://doi.org/10.1016/j.jvolgeores.2016.10.013>.

636 Girona, T., Costa, F., Newhall, C., Taisne, B., 2014. On depressurization of volcanic
637 magma reservoirs by passive degassing. *J. Geophys. Res., Solid Earth* 119(12), 8667-8687,
638 <https://doi.org/10.1002/2014JB011368>.

639 Gurioli, L., Harris, A.J.L., Houghton, B.F., Polacci, M., Ripepe, M., 2008. Textural and
640 geophysical characterization of explosive basaltic activity at Villarrica volcano. *J. Geophys.*
641 *Res., Solid Earth* 113(B8), <https://doi.org/10.1029/2007JB005328>.

642 Gurioli, L., et al., 2015. MeMoVolc consensual document: a review of cross-disciplinary
643 approaches to characterizing small explosive magmatic eruptions. *Bull. Volcanol.* 77,
644 <https://doi.org/10.1007/s00445-015-0935-x>.

645 Hall, M.L., Steele, A.L., Bernard, B., Mothes, P.A., Vallejo, S.X., Douillet, G.A., Ramón,
646 P.A., Aguaiza, S.X., Ruiz, M.C., 2015. Sequential plug formation, disintegration by Vulcanian
647 explosions, and the generation of granular Pyroclastic Density Currents at Tungurahua
648 volcano (2013–2014), Ecuador. *J. Volcanol. Geotherm. Res.* 306, 90-103,
649 <https://doi.org/10.1016/j.jvolgeores.2015.09.009>.

650 Heap, M.J., Farquharson, J.I., Wadsworth, F.B., Kolzenburg, S., Russell, J.K., 2015.
651 Timescales for permeability reduction and strength recovery in densifying magma. *Earth*
652 *Planet. Sci. Lett.* 429, 223-233, <https://doi.org/10.1016/j.epsl.2015.07.053>.

653 Hidalgo, S., Battaglia, J., Arellano, S., Steele, A., Bernard, B., Bourquin, J., Galle, B.,
654 Arrais, S., Vásconez, F., 2015. SO₂ degassing at Tungurahua volcano (Ecuador) between 2007
655 and 2013: Transition from continuous to episodic activity. *J. Volcanol. Geotherm. Res.* 298, 1-
656 14, <https://doi.org/10.1016/j.jvolgeores.2015.03.022>.

657 Johnson, J.B., Aster, R.C., 2005. Relative partitioning of acoustic and seismic energy
658 during strombolian eruptions. *J. Volcanol. Geotherm. Res.* 148, 334-354,
659 <https://doi.org/10.1016/j.jvolgeores.2005.05.002>.

660 Jones, R., Manville, V., Andrade, D., 2015. Probabilistic analysis of rain-triggered lahar
661 initiation at Tungurahua volcano. *Bull. Volcanol.* 77(8), 68, [https://doi.org/10.1007/s00445-](https://doi.org/10.1007/s00445-015-0946-7)
662 015-0946-7.

663 Julian, B.R., 1994. Volcanic tremor: nonlinear excitation by fluid flow. *J. Geophys. Res.*
664 99, 11859-11877, <https://doi.org/10.1029/93JB03129>.

665 Kim, K., Lees, J.M., Ruiz, M.C., 2014. Source mechanism of Vulcanian eruption at
666 Tungurahua Volcano, Ecuador, derived from seismic moment tensor inversions. *J. Geophys.*
667 *Res., Solid Earth* 119, 1145-1164, <https://doi.org/10.1002/2013JB010590>.

668 Kolzenburg, S., Russell, J.K., 2014. Welding of pyroclastic conduit infill:
669 A mechanism for cyclical explosive eruptions, *J. Geophys. Res., Solid Earth* 119, 5305–5323,
670 <https://doi.org/10.1002/2013JB010931>.

671 Kumagai, H., Nakano, M., Maeda, T., Yepes, H., Palacios, P., Ruiz, M., Arrais, S., Vaca,
672 M., Molina, I., Yamashima, T., 2010. Broadband seismic monitoring of active volcanoes using
673 deterministic and stochastic approaches. *J. Geophys. Res., Solid Earth* 115(B8),
674 <https://doi.org/10.1029/2009JB006889>.

675 Le Pennec, J.-L., Jaya, D., Samaniego, P., Ramón, P., Yáñez, S.M., Egred, J., Van Der
676 Plicht, J., 2008. The AD 1300–1700 eruptive periods at Tungurahua volcano, Ecuador,
677 revealed by historical narratives, stratigraphy and radiocarbon dating. *J. Volcanol. Geotherm.*
678 *Res.* 176, 70-81, <https://doi.org/10.1016/j.jvolgeores.2008.05.019>.

679 Lesage, P., Mora, M.M., Alvarado, G.E., Pacheco, J., Métaxian, J.-P., 2006. Complex
680 behavior and source model of the tremor at Arenal volcano, Costa Rica. *J. Volcanol.*
681 *Geotherm. Res.* 157, 49-59, <https://doi.org/10.1016/j.jvolgeores.2006.03.047>.

682 Melnik, O., Barmin, A.A., Sparks, R.S.J., 2005. Dynamics of magma flow inside volcanic
683 conduits with bubble overpressure buildup and gas loss through permeable magma. *J.*
684 *Volcanol. Geotherm. Res.* 143, 53-68, <https://doi.org/10.1016/j.jvolgeores.2004.09.010>.

685 Mothes, P.A., Yepes, H.A., Hall, M.L., Ramón, P.A., Steele, A.L., Ruiz, M.C., 2015. The
686 scientific–community interface over the fifteen-year eruptive episode of Tungurahua Volcano,
687 Ecuador. *Journal of Applied Volcanology* 4(1), 9, <https://doi.org/10.1186/s13617-015-0025-y>.

688 Neuberg, J.W., Collinson, A.S., Mothes, P.A., Ruiz, M.C., Aguaiza, S., 2018.
689 Understanding cyclic seismicity and ground deformation patterns at volcanoes: Intriguing
690 lessons from Tungurahua volcano, Ecuador. *Earth. Planet. Sci. Lett.* 482, 193-200,
691 <https://doi.org/10.1016/j.epsl.2017.10.050>.

692 Ripepe, M., Harris, A.J., Carniel, R., 2002. Thermal, seismic and infrasonic evidences of
693 variable degassing rates at Stromboli volcano. *J. Volcanol. Geotherm. Res.* 118, 285-297,
694 [https://doi.org/10.1016/S0377-0273\(02\)00298-6](https://doi.org/10.1016/S0377-0273(02)00298-6).

695 Ripepe, M., Marchetti, E., Olivieri, G., Harris, A., Dehn, J., Burton, M., Caltabiano, T.,
696 Salerno, G., 2005. Effusive to explosive transition during the 2003 eruption of Stromboli
697 volcano. *Geology* 33, 341-344, <https://doi.org/10.1130/G21173.1>.

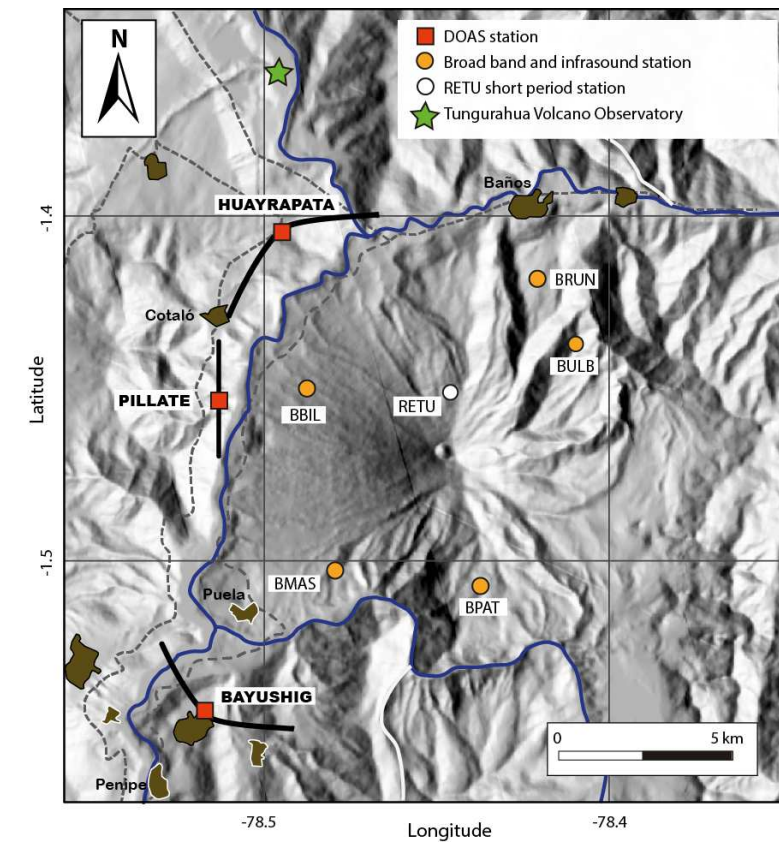
698 Samaniego, P., Le Pennec, J.-L., Robin, C., Hidalgo, S., 2011. Petrological analysis of the
699 pre-eruptive magmatic process prior to the 2006 explosive eruptions at Tungurahua volcano
700 (Ecuador). *J. Volcanol. Geotherm. Res.* 199, 69-84,
701 <https://doi.org/10.1016/j.jvolgeores.2010.10.010>.

702 Vitturi, M.D.M., Clarke, A.B., Neri, A., Voight, B., 2008. Effects of conduit geometry on
703 magma ascent dynamics in dome-forming eruptions. *Earth Planet. Sci. Lett.* 272(3-4), 567-
704 578, <https://doi.org/10.1016/j.epsl.2008.05.025>.

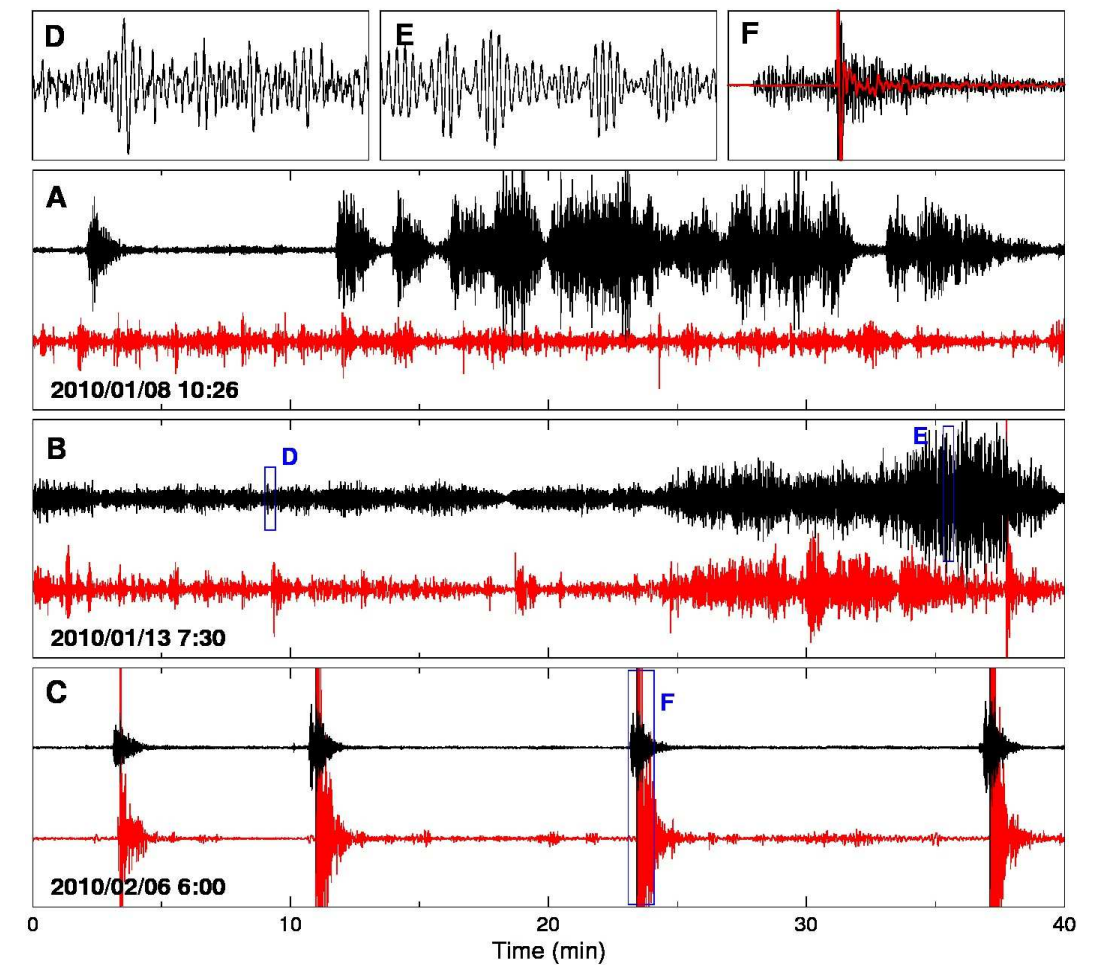
705 Watt, S.F.L., Mather, T. A., Pyle, D.M., 2007. Vulcanian explosion cycles: Patterns and
706 predictability. *Geology* 35 (9), 839-842, doi:10.1130/G23562A.1.

707 Wright, H., Cashman, K., Mothes, P., Hall, M.L., Ruiz, A., and Le Pennec, J.-L., 2012.
708 Estimating rates of decompression from textures of erupted ash particles produced by 1999-
709 2006 eruptions of Tungurahua volcano, Ecuador. *Geology* 40, 619-622,
710 <https://doi.org/10.1130/G32948.1>.

711

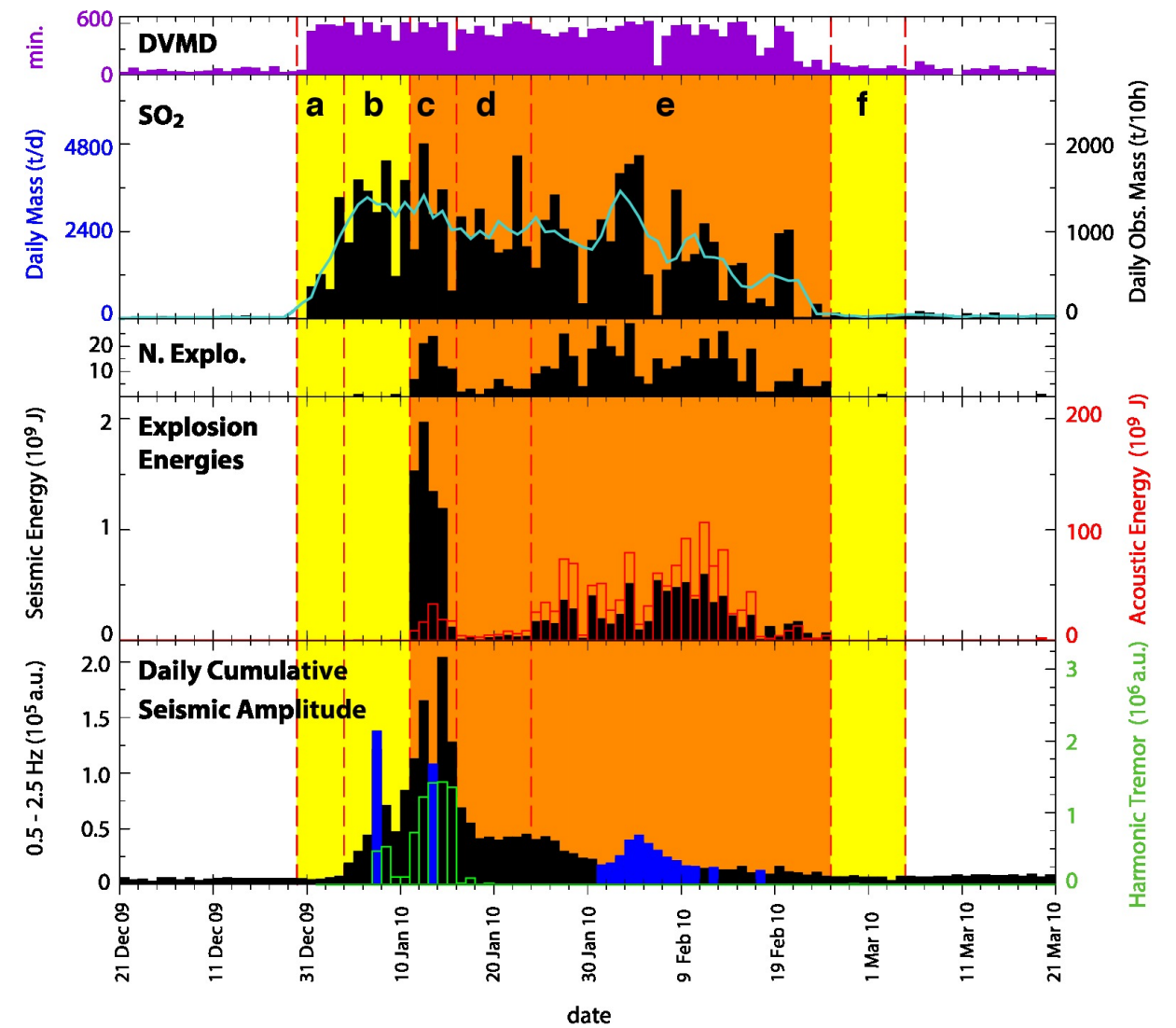


712
 713 **Figure 1:** Map of Tungurahua volcano showing the location of the three scanning-DOAS
 714 stations, five broadband seismic/infrasound stations and one short-period seismic station
 715 RETU whose data was used for this study.



716
717 **Figure 2:** Seismic -vertical component- (black) and acoustic (red) signals recorded at station
718 BMAS. Plots (A), (B) and (C) show 40-min seismic and acoustic waveforms illustrating three
719 different types of eruptive activity starting at the times specified in the lower left corners. On
720 these 3 plots, seismic and acoustic traces have respectively common vertical scales and the
721 amplitude of acoustic traces have been divided by a factor 100. (A) Tremor bursts, mostly
722 harmonic, recorded during Strombolian activity in episode (b), (B) harmonic and non-
723 harmonic tremor bursts during episode (c) and (C) strong Vulcanian explosions and low
724 background tremor during episode (e). Plots (D) and (E) detail two 24-s windows showing
725 respectively examples of seismic recordings for non-harmonic and harmonic tremor. Plot (F)
726 shows a 60-s time frame for a seismic explosion quake with its corresponding acoustic signal.

727 All three time frames are extracted from the signals shown in plots (B) and (C) at the
728 corresponding locations shown within blue rectangles.



730

731 **Figure 3:** Comparison of geophysical time-series. Onset and ending times of the six episodes

732 (a) to (f), described in the text, are delimited by vertical red dashed lines. HEA and LEA

733 periods are displayed in yellow and orange background colors, respectively. “Daily

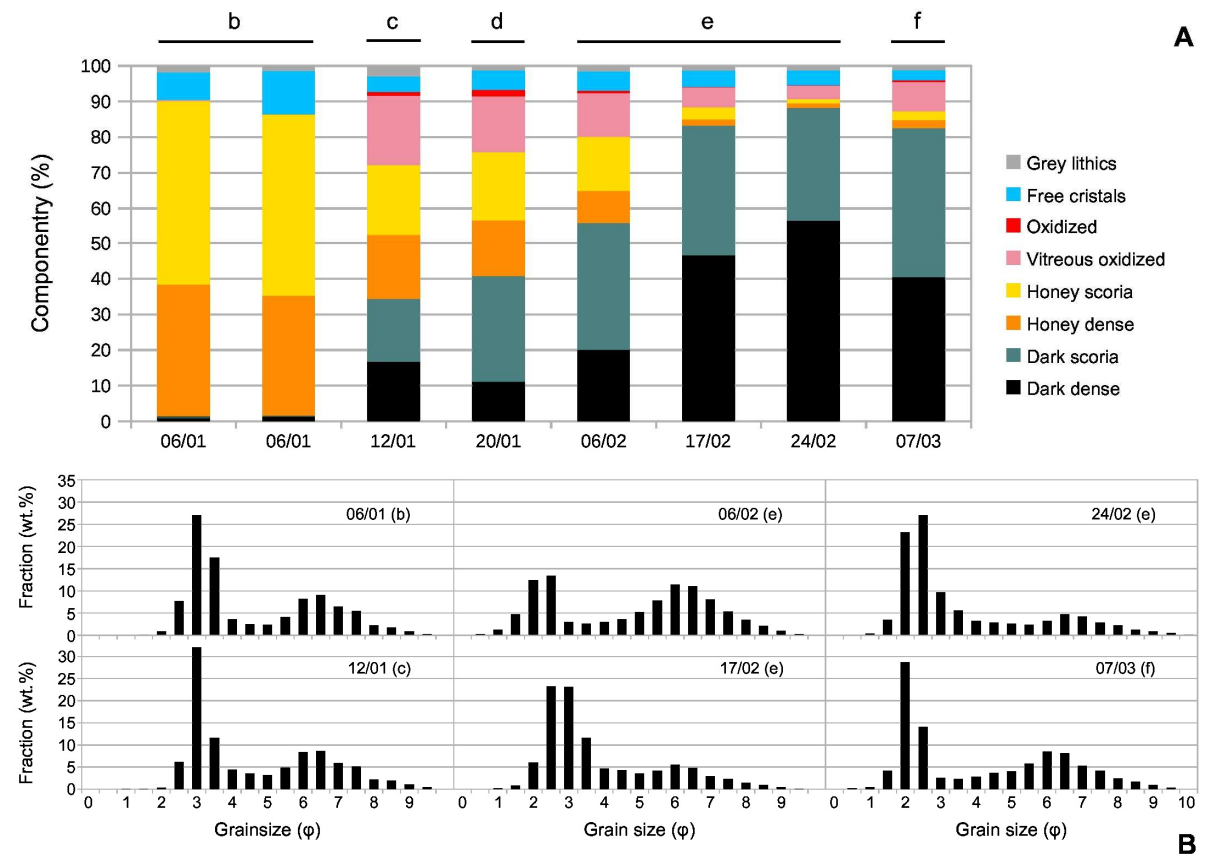
734 Cumulated Seismic Amplitude” shows the daily cumulative values of the Median Seismic

735 Amplitude (MSA) for the full short-period range at station RETU (black), completed with

736 scaled data from BMAS (blue) when station RETU was down or saturated. “Explosions

737 Energies” shows daily cumulative values of the seismic (black) and acoustic (red) energies for

738 the significant explosions. The vertical scale for acoustic energy is exactly 100 times that of
739 seismic so that the reader can directly compare the energies with respect to the threshold value
740 of 100 mentioned in the text. “N. Explo.” displays the daily number of significant explosions.
741 “SO₂” shows the daily Observed Mass of SO₂ with the averaged values calculated over 5-d
742 sliding windows shown in turquoise. “DVMD” shows the Daily Valid Measurement Duration,
743 i.e. the number of minutes of valid SO₂ measurements. All three scanning-DOAS stations
744 were functioning properly during the study period. Figure 5 shows sketches presenting a
745 model of conduit dynamics corresponding to the six episodes.



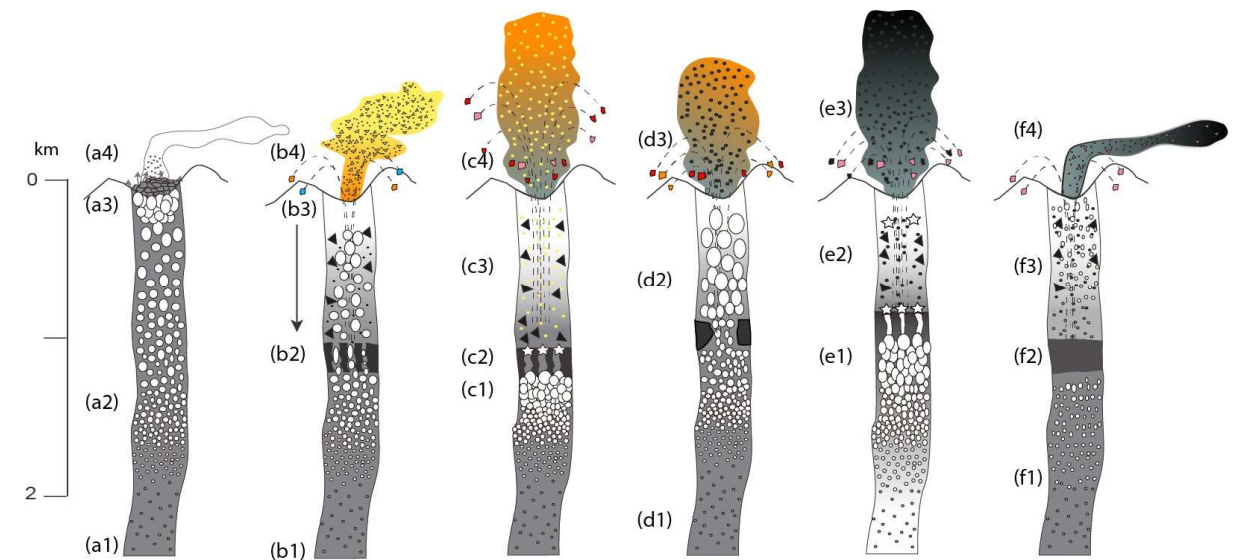
747

748 **Figure 4:** A) Barplots of the componentry and B) histograms of the grain-size distribution of

749 ash samples collected during the December 2009-March 2010 eruption. Description of the

750 components is given in the text. $\phi = -\log_2 D$ where D is the particle diameter in millimeters. b,

751 c, d, e, f correspond to the eruptive episodes described in the text.



752

753 **Figure 5:** Sketches showing a model of conduit dynamics for the six episodes of activity
 754 defined in the text. Annotations along the sketches describe the characteristics of each activity
 755 from bottom to top. (a1) New magma input, (a2) gas easily exsolved, (a3) high gas pressure
 756 at the base of the lava accumulation in the crater, (a4) gas and ash venting. (b1) Steady arrival
 757 of magma, (b2) generation of a dense, gas depleted zone, (b3) destruction of the lava
 758 accumulation in the crater, (b4) gas and ash venting with Strombolian activity, emissions
 759 dominated by honey-color juvenile material. (c1) Gas accumulation below the dense zone,
 760 (c2) cyclical breaking of the dense zone, explosive release of gas, (c3) gas transport of
 761 juvenile material and cleaning of the conduit, (c4) gas and ash venting, Strombolian and
 762 Vulcanian activity. (d1) New magma injection with the same composition, (d2) mixed
 763 fragmentation process, (d3) steady ash column. (e1) same as (c2), (e2) gas transport of
 764 juvenile material with decreasing recycling, (e3) transition toward a more purely Vulcanian
 765 eruptive process. (f1) No more gas arrival, (f2) the dense zone cools down and forms a plug,
 766 (f3) remnant gas leaving the conduit, (f4) low gas and ash emission.